SANDIA REPORT

SAND2004-5686
Unlimited Release
Printed November 2004

Adaptive Optics and Phase Diversity Imaging for Responsive Space Applications

Mark W. Smith
David V. Wick

Prepared by
Sandia National Laboratories
Albuquerque, New Mexico 87185 and Livermore, California 94550

Sandia is a multiprogram laboratory operated by Sandia Corporation,
a Lockheed Martin Company, for the United States Department of Energy's
National Nuclear Security Administration under Contract DE-AC04-94AL85000.

Issued by Sandia National Laboratories, operated for the United States Department of Energy by Sandia Corporation.

Available to DOE and DOE contractors from
U.S. Department of Energy
Office of Scientific and Technical Information
P.O. Box 62
Oak Ridge, TN 37831

Telephone: (865)576-8401
Facsimile: (865)576-5728
E-Mail: reports@adonis.osti.gov
Online ordering: http://www.osti.gov/bridge

Available to the public from
U.S. Department of Commerce
National Technical Information Service
5285 Port Royal Rd
Springfield, VA 22161

Telephone: (800)553-6847
Facsimile: (703)605-6900
E-Mail: orders@ntis.fedworld.gov
Online order: http://www.ntis.gov/help/ordermethods.asp?loc=7-4-0#online

SAND2004-5686
Unclassified, Unlimited Release
November 2004

Adaptive Optics and Phase Diversity Imaging for Responsive Space Applications

Mark W. Smith
Remote Sensing and Exploitation

David V. Wick
Computational Initiatives

Sandia National Laboratories
P.O. Box 5800
Albuquerque, NM 87185-0570

Abstract

The combination of phase diversity and adaptive optics offers great flexibility. Phase diverse images can be used to diagnose aberrations and then provide feedback control to the optics to correct the aberrations. Alternatively, phase diversity can be used to partially compensate for aberrations during post-detection image processing. The adaptive optic can produce simple defocus or more complex types of phase diversity. This report presents an analysis, based on numerical simulations, of the efficiency of different modes of phase diversity with respect to compensating for specific aberrations during post-processing. It also comments on the efficiency of post-processing versus direct aberration correction. The construction of a bench top optical system that uses a membrane mirror as an active optic is described. The results of characterization tests performed on the bench top optical system are presented. The work described in this report was conducted to explore the use of adaptive optics and phase diversity imaging for responsive space applications.

Keywords: phase diversity, adaptive optics, imaging system, image restoration

This page intentionally left blank

Contents

Figures

Tables

1. Introduction

Phase diversity imaging refers to the technique of applying intentional phase perturbations to wave fronts while acquiring multiple images of a single scene. The use of phase diversity in optical imaging was evidently first proposed by R. A. Gonsalves,[1] who suggested using a pair of images, one in-focus and one slightly out-of-focus, to jointly estimate the phase errors across the pupil of an imaging system and the intensity distribution of the object. Knowledge of the phase errors would then be used to provide real-time feedback control to active optics or to drive image reconstruction at a post-processing stage. A large body of literature devoted to phase diversity imaging has developed over the intervening years. S. M. Jefferies and coworkers have recently published an article with a good list of references.[2] The use of diversity imaging to enhance the modulation transfer function (MTF) and channel capacity (CC) of an aberrated imaging system has also been explored.[3-5]

Diversity imaging and active optics are very complementary and offer a variety of possibilities when used in combination. The active optic can introduce the phase diversity. The phase diversity may be a simple defocus, which corresponds to a quadratic variation of phase across the exit pupil, or it may be much more general and complex. The phase diversity may be used either to diagnose aberrations and provide feedback control to the active optics, or to improve the quality of image reconstructions during a post-processing stage.

Figure 1 shows a generic concept for an imaging system that uses an active optic as part of a three-tiered approach to forming a good-quality image. The first element of the system is a primary optic that, due either to cost constraints or technical constraints, suffers from several waves of aberration. The second element is an active optic that partially corrects the aberrations. The third element is a diversity imaging scheme that improves the quality of the final reconstructed image.

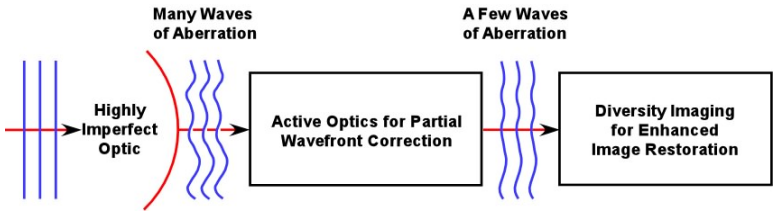

Figure 1. Schematic Diagram of a Three-Tiered Hybrid Imaging System.

Figure 2 illustrates the use of diversity imaging to enhance the MTF of a system, using as an example diverse defocus applied to third-order spherical aberration (SA). When defocus is approximated as a quadratic variation in phase, the total phase error for spherical aberration plus defocus can be expressed as

$$\Phi = A(\rho^4 + B\rho^2)\lambda\,, \qquad (1)$$

where

Φ = the wave front aberration in units of wavelength,

ρ = a normalized radial coordinate ($0 \le \rho \le 1.0$) in the exit pupil,

A = the spherical aberration coefficient,

B = the relative defocus coefficient, and

λ = the wavelength.

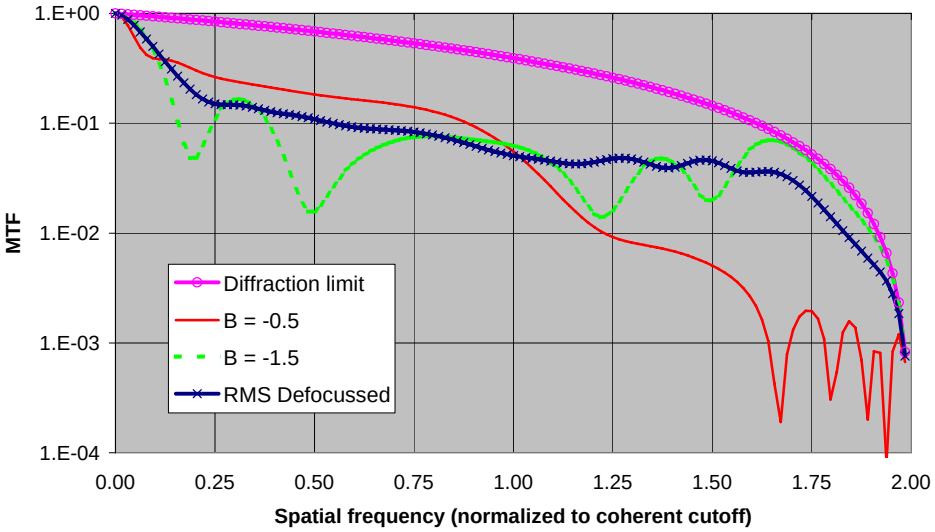

Figure 2. MTF for Four Waves of Spherical Aberration for B = –0.5 and –1.5; the RMS MTF for B = –0.5, –1.0, –1.25, –1.5; and the Diffraction-Limited MTF.

Figure 2 shows MTF calculations for four waves of third-order SA plus variable defocus. The diffraction-limited MTF is shown for comparison. The circle-of-least-confusion MTF (B = –1.5) provides the best performance at higher spatial frequencies. The near-paraxial MTF (B = –0.5) is essentially a low pass filter. Figure 2 also shows the root-mean-square (RMS) MTF that results when the following defocus settings are combined in equal weights: B = –0.5, –1.0, –1.25, –1.5.

The MTF for any single focus setting of an aberrated system may fall to zero, or to very low values, at various spatial frequencies. However, the MTF may be appreciably greater than zero at these same spatial frequencies at a different focus setting (i.e., with a different phase perturbation applied to the wave fronts). By collecting multiple frames of data at different focus/phase settings, a composite MTF can be produced that is more uniform as a function of spatial frequency. As long as the signal power of the corresponding composite image can be kept significantly higher than the noise power at a given spatial frequency, useful information will be present at that frequency, and that information can contribute to a reconstructed image.

The work presented in this report deals purely with the issue of maximizing the potential for post-processing reconstructions, based on the assumption that knowledge of the system aberrations has already been obtained. Most of the work consists of an analysis, using numerical simulations, of the efficiency of using different modes of phase diversity to compensate for specific aberrations. Comments are also made on the efficiency of post-processing versus direct aberration correction.

A description of a bench top optics system that was developed is also presented. The intended use of this bench top system was to produce quantitative image data that would be used to validate the computer simulations of the diversity imaging. However, the results that were

actually obtained with this system were limited to characterizations of baseline system performance, without the introduction of aberrations or phase diversity.

2. Methods Used for Numerical Simulations

2.1 Point Spread Function and MTF Calculations

All numerical simulations were carried out using MATLAB™. Point spread functions (PSFs) were calculated using the standard approximations of scalar diffraction theory in the Fraunhoffer regime.[6] A circular exit pupil and quasi-monochromatic, incoherent illumination were assumed. Various phase perturbations were defined over the domain of the pupil, and two-dimensional (2-D) fast Fourier transform (FFT) routines were then used to calculate the coherent PSF for each prescribed phase. The incoherent PSF was then calculated as the absolute value squared of the coherent PSF. The incoherent optical transfer function (OTF) was calculated as the 2-D FFT of the incoherent PSF. The incoherent modulation transfer function (MTF) was calculated as the absolute value of the incoherent OTF.

A mathematical description of the pupil function is

$$U(\rho,\theta) = T(\rho,\theta)\exp[i\Phi(\rho,\theta)]\,, \qquad (2)$$

where

U = the complex product of a real transmission function and a complex phase function,

T = the real-valued transmission function,

ρ = a normalized radial coordinate ($0 \le \rho \le 1.0$),

θ = an angular coordinate, and

Φ = the departure of the wave front from a reference sphere, in units of radians. In this investigation, Φ is the sum of a fixed aberration term and a variable phase diversity term.

2.2 Choice of Aberrations and Diversity Modes

Both the aberrations and the modes of phase diversity were described using Zernike polynomials, for which there are various numbering conventions. The convention used by ZEMAX™ for the Zernike standard polynomial set was adopted for this work. These polynomials and their indices under this convention are listed in Table 1. With the normalization factors shown in Table 1, the amplitude coefficient for each polynomial gives directly the contribution of this term to the RMS wave front error.

The complete set of Zernike polynomials contains both sine and cosine terms. Only the cosine terms, plus the terms with no angular dependence, were used to describe the aberrations. Because the aberrations were studied as individual modes rather than as combinations of modes, this created no loss of generality—it simply corresponds to a particular orientation of the coordinates. However, both the sine and cosine terms were used for the phase diversity modes. This is equivalent to allowing rotation of the phase diversity modes relative to the aberrations.

Table 1. List of Indices and Functional Forms of Zernike Polynomials.

INDEX	ZERNIKE POLYNOMIAL		INDEX	ZERNIKE POLYNOMIAL
1	1		15	sqrt(10) $\rho^4 \sin(4\theta)$
2	sqrt(4) $\rho \cos(\theta)$		16	sqrt(12) $(10\rho^5 - 12\rho^3 + 3\rho) \cos(\theta)$
3	sqrt(4) $\rho \sin(\theta)$		17	sqrt(12) $(10\rho^5 - 12\rho^3 + 3\rho) \sin(\theta)$
4	sqrt(3) $(2\rho^2 - 1)$		18	sqrt(12) $(5\rho^5 - 4\rho^3) \cos(3\theta)$
5	sqrt(6) $\rho^2 \sin(2\theta)$		19	sqrt(12) $(5\rho^5 - 4\rho^3) \sin(3\theta)$
6	sqrt(6) $\rho^2 \cos(2\theta)$		20	sqrt(12) $\rho^5 \cos(5\theta)$
7	sqrt(8) $(3\rho^3 - 2\rho) \sin(\theta)$		21	sqrt(12) $\rho^5 \sin(5\theta)$
8	sqrt(8) $(3\rho^3 - 2\rho) \cos(\theta)$		22	sqrt(7) $(20\rho^6 - 30\rho^4 + 12\rho^2 - 1)$
9	sqrt(8) $\rho^3 \sin(3\theta)$		23	sqrt(14) $(15\rho^6 - 20\rho^4 + 6\rho^2) \sin(2\theta)$
10	sqrt(8) $\rho^3 \cos(3\theta)$		24	sqrt(14) $(15\rho^6 - 20\rho^4 + 6\rho^2) \cos(2\theta)$
11	sqrt(5) $(6\rho^4 - 6\rho^2 + 1)$		25	sqrt(14) $(6\rho^6 - 5\rho^4) \sin(4\theta)$
12	sqrt(10) $(4\rho^4 - 3\rho^2) \cos(2\theta)$		26	sqrt(14) $(6\rho^6 - 5\rho^4) \cos(4\theta)$
13	sqrt(10) $(4\rho^4 - 3\rho^2) \sin(2\theta)$		27	sqrt(14) $\rho^6 \sin(6\theta)$
14	sqrt(10) $\rho^4 \cos(4\theta)$		28	sqrt(14) $\rho^6 \cos(6\theta)$

2.3 Choice of Optimization Metric

Any optimization problem requires the choice of a merit function that is to be maximized, or alternatively the choice of a cost function that is to be minimized. There is no established standard, nor an obvious choice, for the merit function to use when optimizing non-quadratic phase diversity.

Two different optimization metrics were explored. The first metric was the minimum value of the MTF. That is, the settings and weights of the phase diversity modes were chosen so that the minimum value of the MTF would be a maximum, relative to the diffraction limit. This can be described as the "keeping your head above water" approach. The idea is that so long as the MTF passes a spatial frequency with an amplitude that is significant compared to the noise floor, then the true amplitude of that spatial frequency can be approximately restored during the image reconstruction step. Mathematically the minimum MTF merit function was defined as

$$MM = \log_{10}(\min(MTF_{abr}/MTF_{dif})) , \qquad (3)$$

where

MM = the minimum MTF merit function,

min = the operation of taking the minimum value as a function of spatial frequency,

MTF_{abr} = the MTF for the aberrated system plus a phase perturbation, and

MTF_{dif} = the diffraction-limited MTF of the system.

The minimum MTF merit function varied relatively rapidly as a function of the amount of phase perturbation that was applied. It also contained many local maxima and minima. This is shown in Figure 3, which plots the minimum MTF for spherical aberration (Zernike mode 11) as a function of defocus (Zernike mode 4).

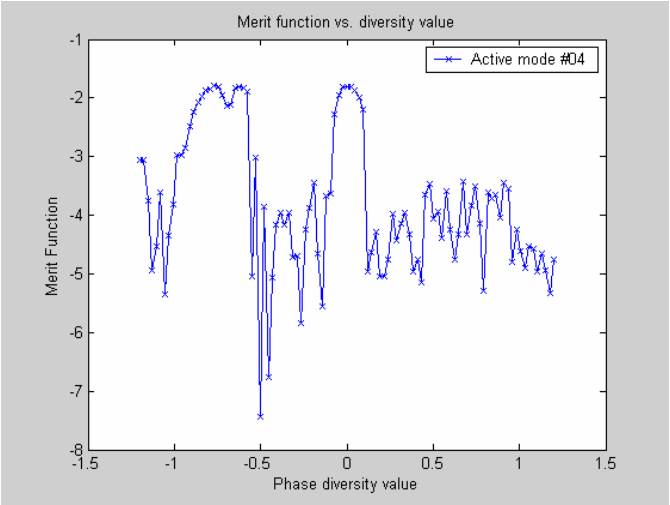

Figure 3. Merit Function Based on Minimum MTF for Spherical Aberration Plus Defocus.

The second metric was based on the channel capacity of the imaging system. Channel capacity is related to the joint information that is present between an image, which has been degraded by blurring and noise, and the corresponding true object. The channel capacity of an additive Gaussian channel in units of bits is[7]

$$CC = \tfrac{1}{2} \log_2(1 + SNR) , \qquad (4)$$

where

CC = the channel capacity in units of bits, and

SNR = the signal-to-noise ratio of the channel.

In order to create a merit function based on channel capacity each spatial frequency element of the 2-D MTF array was treated as a discrete channel. The SNR for each such channel was calculated as the product of the SNR for the zero frequency, or DC, component times the value of the MTF at each spatial frequency. The channel capacity for a given spatial frequency element is then

$$CC(\nu) = \tfrac{1}{2} \log_2(1 + SNR_{DC} \times MTF(\nu)) , \qquad (5)$$

where

$CC(\nu)$ = the channel capacity for spatial frequency element ν,

SNR_{DC} = the SNR for the zero frequency component, and

$MTF(\nu)$ = the MTF at frequency ν.

A cost function was created by summing over all spatial frequencies the difference between the CC for the aberrated system (with phase diversity applied) and the CC for a diffraction-limited

system. SNR_{DC} was set equal to 100 for all calculations. The absolute value of CC(ν) for a given MTF(ν) depends in general on SNR_{DC}. However, working with the difference between the CC for the aberrated system and the CC for a diffraction-limited system suppresses the effect of the exact value of the SNR. When the product $SNR_{DC} \times MTF(\nu)$ is large compared to 1, the channel capacity becomes approximately

$$CC(\nu) \approx \tfrac{1}{2} [\log_2(SNR_{DC}) + \log_2(MTF(\nu))] \, . \qquad (\mathbf{6})$$

In this limit, $\tfrac{1}{2} \log_2(SNR_{DC})$ is simply a constant additive term. Since the same SNR_{DC} is assumed for the diffraction limited and aberrated systems, this term vanishes when the abberated CC is subtracted from the diffraction limited CC.

To create a merit function the channel capacity cost function was normalized by the total channel capacity of a diffraction limited system and the result was subtracted from 1. This creates a merit function that ranges from 0 (zero channel capacity) to 1 (channel capacity equal to the diffraction limit). Figure 4 shows the CC merit function for spherical aberration (Zernike mode 11) as a function of defocus (Zernike mode 4). This merit function still contains local maxima and minima, but it is much less jagged than the MM merit function. The CC merit function was therefore chosen for the optimizations.

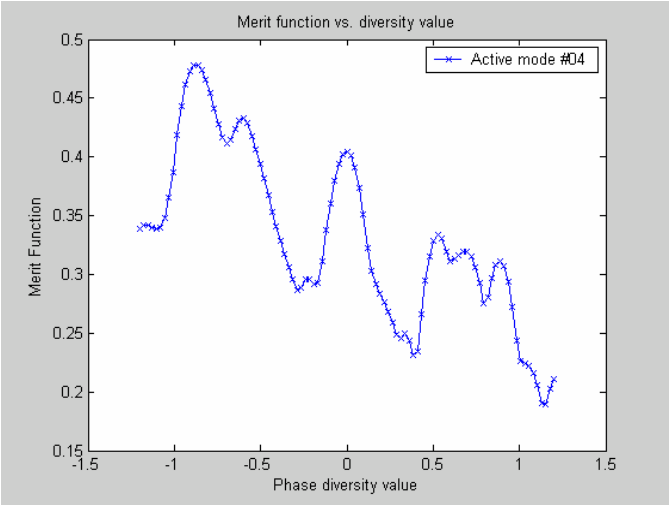

Figure 4. Merit Function Based on Channel Capacity for Spherical Aberration Plus Defocus.

2.4 Optimization Algorithm

Optimization was carried out using precomputed sets of MTFs. A single set of MTFs was created for each of the following Zernike aberration modes: 6, 8, 10, 11, 12, 14, 16, 18, 20, 22, 24, 26, and 28 for each of the following amplitudes: 1/14, 2/14, 4/14, and 8/14 waves. Recall that the RMS wave front error for each Zernike polynomial is equal to the amplitude. The amplitudes above are listed in units of N/14 waves since one criterion for a well corrected optical system is to have an RMS wave front error of no more than 1/14 of a wavelength.[8] Within each set, MTFs were computed for a range of amplitudes for each of the following diversity modes: 4, 5, 6, 9, 10, 14, 15, 20, 21, 27, and 28. Each precomputed set of MTFs was therefore a two-dimensional array (diversity mode and amplitude) of two-dimensional MTFs, or a four-dimensional array in aggregate.

While the precomputed MTF sets contained all of the diversity modes listed above, optimization was restricted to various subsets of these modes. Four different sets of phase diversity modes were used. The first was the single best amplitude of mode 4, which corresponds to the single best focus. The second set was diverse amplitudes of mode 4, which corresponds to the usual practice of using defocus diversity only. The third set was diverse amplitudes of modes 4, 5, 6, 9, and 10. This will be referred to as the low-mode set. The fourth set was diverse settings of modes 14, 15, 20, 21, 27, and 28. This will be referred to as the high mode set. With the exception of mode 4, all of the modes for the low mode and high mode sets were chosen to a have a zero Laplacian ($\nabla^2\Phi = 0$). This means that these are the normal modes of static deflection for a membrane,[9] and hence it should be relatively easy to produce these modes using a membrane mirror as the active optic.

A three step algorithm was used for the optimizations. The first step was to find the single best diversity mode from a given set, and the best amplitude for that mode, for each aberration. This could be called optimizing a single degree of phase diversity freedom. The second step was to add successive degrees of freedom, and to optimize for an additional mode, amplitude, and weighting factor of phase diversity at each stage. The weighting factors correspond to the fractional amount of dwell time devoted to obtaining an image for a particular mode and amplitude of phase diversity. The weighting factors were always required to sum to 1.0, which corresponds to maintaining a fixed total period for data acquisition. The third and final step was to reoptimize the weighting factors, using a multi-dimensional optimization algorithm, after all of the most promising modes and amplitudes of phase diversity had been identified at step two.

Optimization of modes and amplitudes was always carried out as an exhaustive search through the first two dimensions of each precomputed set of MTFs. The weighting factor for each mode and amplitude was allowed to vary continuously between 0.0 (mode not used at all) and 1.0 (mode used exclusively).

2.5 Image Simulations

The input scene was an image of a region of Washington DC that was obtained by the IKONOS satellite operated by Space Imaging (http://www.spaceimaging.com). The original image was converted from color to black and white and was then down-sampled by a factor of two to sharpen the edges in the image. To create a diffraction-limited image, the scene was Fourier transformed, and the resulting spectrum was multiplied by the OTF for a diffraction-limited system. The incoherent cutoff frequency for the diffraction-limited OTF was set equal to the Nyquist frequency for the original scene. An inverse Fourier transform was then used to produce the diffraction-limited image from the diffraction-limited spatial frequency spectrum. The same procedure was used to create aberrated scenes, except that aberrated OTF's were used. After the images were blurred, Poisson noise was added. A mean SNR_{DC} of 100:1 was used for all cases. To provide for a fair comparison between the single-frame best focus results and the multi-frame phase diverse results, the root-squared-sum (RSS) SNR_{DC} was maintained at the fixed value of 100 when multiple frames were used. This is equivalent to maintaining a fixed total time for data collection. A multi-frame Wiener-Helstrom filter was used for the image reconstructions.[3,10]

This page intentionally left blank

3. Results of Numerical Simulations

3.1 Optimized Channel Capacity for Various Conditions

Figure 5 summarizes the results of the channel capacity (CC) optimizations for aberrations with a Zernike mode amplitude of 4/14 waves. Results are shown for the single best focus, for defocus (quadratic) diversity only, for the low-mode set of generalized (non-quadratic) phase diversity, and for the high-mode set of generalized phase diversity. Results are shown only for aberration modes that are different than the phase diversity modes, since using the same modes for both would be tantamount to aberration correction, not phase diverse image collection. For each mode and amplitude of aberration, the channel capacity results obey the following relationship:

$$CC_{lm} \geq CC_{dd} \geq CC_{bf} , \qquad (7)$$

where CC_{lm} is the CC of the low-mode set of generalized phase diversity, CC_{dd} is the CC for defocus diversity, and CC_{bf} is the CC for the single best focus setting.

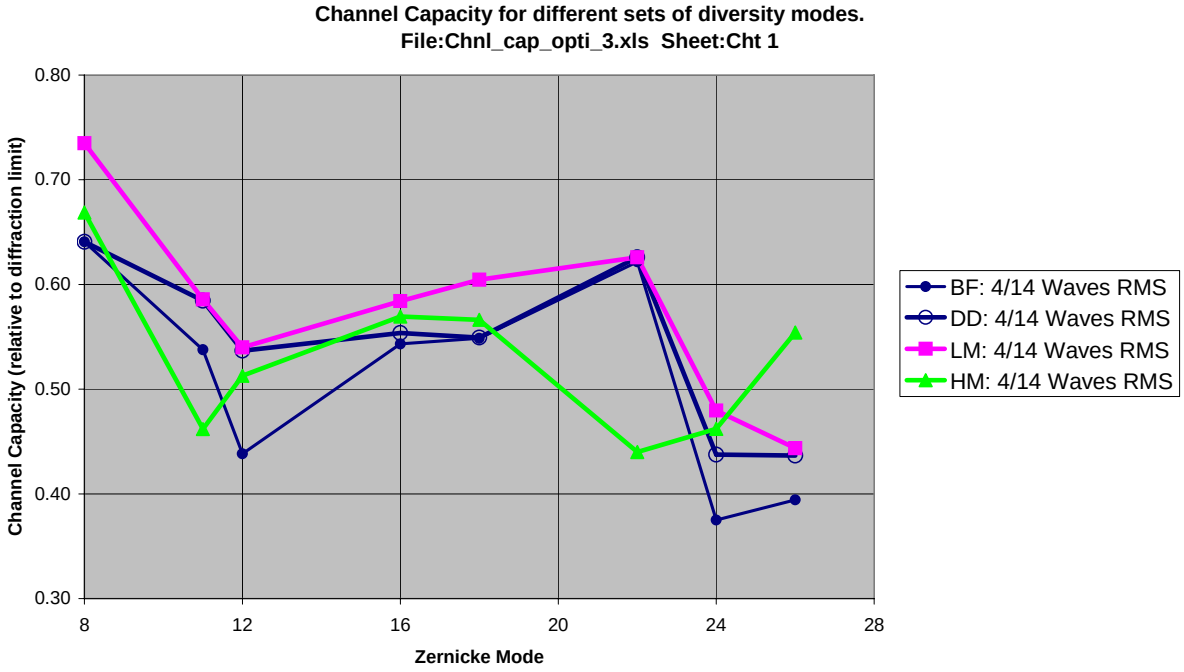

Figure 5. Results of CC Optimization for Different Types of Phase Diversity. BF is the best focus, DD is the defocus diversity, LM is the low-mode diversity, and HM is the high-mode diversity.

Defocus diversity is generally better than the single best focus, and the low-mode non-quadratic diversity is better still. The low-mode set of non-quadratic phase diversity produces better results than does the high-mode set, except in the case of aberration mode 26.

Close inspection of the best focus and defocus diversity lines in Figure 5 shows that the two yield almost identical results for Zernike modes 8, 16, 18, and 22, whereas defocus diversity is superior to the single best focus for diversity modes 11, 12, 24, and 26. Table 1 shows that mode 11 does not depend on the azimuth angle, modes 12 and 24 vary as $\cos(2\theta)$, and mode 26 varies as $\cos(4\theta)$. All of these modes vary as an even power of the azimuth angle, θ, and defocus

diversity is effective in improving the channel capacity for all of these modes. On the other hand, Table 1 shows that modes 8 and 16 vary as cos(θ), and mode 18 varies as cos(3θ). Defocus diversity provides no improvement over the single best focus setting for these modes that vary as an odd power of the azimuth angle. The one exception to this pattern is mode 22, which does not depend on the azimuth angle, but which also shows no improvement for defocus diversity versus single best focus.

Figure 6 shows a comparison of the optimization results for single best focus and for low-mode generalized diversity for aberration amplitudes of 1/14, 2/14, 4/14, and 8/14 waves. Recall that a well-corrected optical system has a maximum RMS wavefront error of 1/14 wave. For this level of aberration, the CC at best focus is >90% of the CC for a diffraction-limited system. For small amounts of aberration, there is not much difference between the CC at best focus and with generalized phase diversity. As the amount of aberration increases, the CC with generalized phase diversity becomes increasingly superior to the CC for the single best focus.

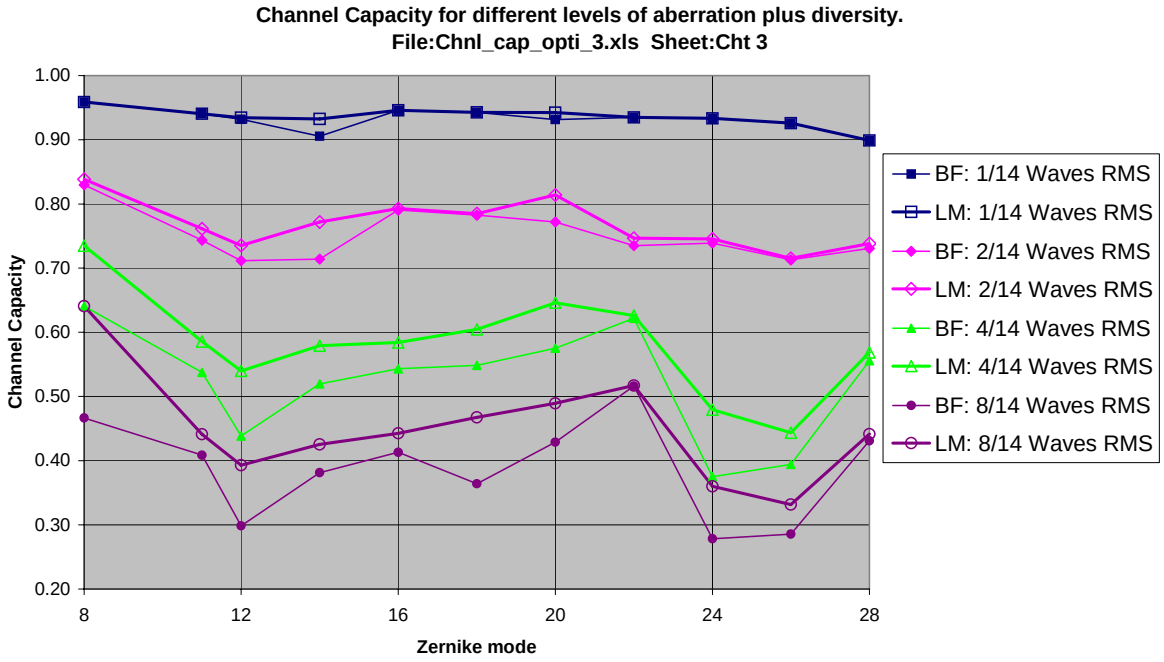

Figure 6. Results of CC Optimization for Best Focus and Low-mode Generalized Diversity for Aberration Amplitudes of 1/14, 2/14, 4/14, and 8/14 Waves.

3.2 Diversity Settings and Weights

Table 2 shows the optimized diversity modes, amplitudes, and weights for various aberrations. Each aberration has an amplitude of 4/14 waves. The optimization was carried out for a total of six diversity settings. The mode values, for both the aberrations and the phase diversity, correspond to the Zernike mode indices shown in Table 1. The diversity amplitude values are in RMS waves.

Table 2 shows several interesting results. For Zernike mode 8 (coma), there is a single phase setting that has a weight of 100%, and every other phase setting has a weight of 0%. This means that the optimum observation strategy for coma is to spend 100% of the available dwell time collecting data from the single best phase setting. Because only a single mode and amplitude are

used rather than multiple settings, this amounts to partially correcting the aberration rather than making use of multiple MTFs.

On the other hand, Table 2 shows that several diversity settings have nonzero weights for Zernike mode 11 (spherical aberration). This indicates that multiple, diverse phase settings are useful when applied to spherical aberration. Mode 4, or defocus, is the main phase diversity mode that is optimal in combination with spherical aberration. Mode 9 adds an additional small contribution with a weight of 11.7%.

Table 2. Phase Diversity Modes, Amplitudes, and Weights Optimized over Six Diversity Settings for Various Zernike Mode Aberrations, Each Having an Amplitude of 4/14 Waves.

ABBR. MODE ⇓	DIVERSITY TERM ⇒	1	2	3	4	5	6
8	Mode : Amp	10: 0.240	4: –0.857	4: –0.857	4: –0.857	4: –0.857	4: –0.857
	Weight	100.0%	0.0%	0.0%	0.0%	0.0%	0.0%
11	Mode : Amp	4: -0.583	4: -0.309	9: 0.189	4: 0.309	4: 0.566	4: -0.583
	Weight	36.8%	29.4%	11.7%	9.9%	6.2%	6.0%
12	Mode : Amp	6: -0.171	4: 0.411	4: -0.429	4: 0.240	4: -0.274	6: 0.420
	Weight	16.9%	21.5%	19.8%	13.9%	13.6%	14.3%
14	Mode : Amp	5: -0.154	5: -0.051	5: -0.257	4: -0.154	5: -0.223	5: -0.137
	Weight	0.0%	7.6%	15.1%	17.0%	17.8%	42.5%
16	Mode : Amp	9: 0.103	10: 0.171	10: -0.154	9: -0.171	10: 0.171	9: -0.171
	Weight	16.1%	29.7%	20.3%	18.3%	11.9%	3.7%
18	Mode : Amp	10: 0.411	10: -0.051	10: -0.771	10: 0.446	10: -0.583	10: 0.429
	Weight	0.0%	24.7%	2.6%	0.0%	3.1%	69.6%
20	Mode : Amp	9: -0.274	10: 0.343	10: -0.377	9: -0.446	10: 0.360	10: -0.360
	Weight	65.3%	3.8%	8.2%	12.3%	8.3%	2.1%
22	Mode : Amp	4: 0.309	4: -0.823	4: 0.326	4: -0.823	4: 0.326	4: -0.823
	Weight	0.0%	5.7%	52.2%	0.4%	39.1%	2.5%
24	Mode : Amp	6: 0.189	5: 0.274	5: -0.274	4: 0.651	4: -0.651	6: -0.103
	Weight	47.3%	17.6%	17.6%	4.6%	4.6%	8.3%
26	Mode : Amp	10: -0.377	4: -0.394	5: 0.206	4: 0.394	9: -0.309	4: 0.137
	Weight	10.8%	21.1%	21.7%	20.6%	15.7%	10.1%
28	Mode : Amp	9: -0.069	6: -0.120	5: -0.103	6: 0.086	5: 0.069	6: -0.051
	Weight	11.2%	0.8%	15.1%	24.4%	17.6%	30.9%

Generally speaking, for a given aberration, only one or two phase diversity modes make a substantial contribution. In some cases the optimization algorithm chose the exact same mode and amplitude for different terms. For aberration mode 16 the diversity mode 10 with an amplitude of 0.171 was chosen for terms 2 and 5, and the diversity mode 9 with an amplitude of –0.171 was chosen for terms 4 and 6.

For the more complicated aberration modes (with higher Zernike polynomial indices) the optimization algorithm tended to select a greater assortment of phase diversity modes. For example, phase diversity modes 10, 4, 5, and 9 are used for aberration mode 26. Another interesting result shows up for mode 24. In this case, equally weighted contributions of opposite

sign are optimum for both of the diversity modes 4 and 5, while mode 6 is used with opposite signs but with asymmetrical amplitudes and weights.

3.3 Simulated Image Reconstructions

Figures 7–11 show a set of image reconstruction results for the IKONOS image that was described in section 2.5. Only diversity settings with an optimized weight greater than 5% were used in the reconstructions. Poisson noise, with an RSS SNR_{DC} of 100:1, was used for each case. A Wiener-Helstrom inverse filter[3,10] was applied to all images. Figure 7 shows the test scene as it would be imaged by a diffraction-limited system whose incoherent cutoff frequency equals the Nyquist frequency for the pixel spacing.

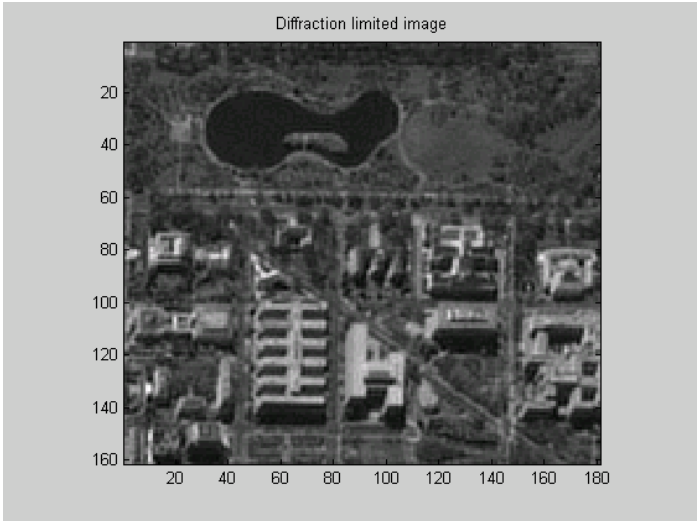

Figure 7. Simulated Image for Diffraction-Limited System.

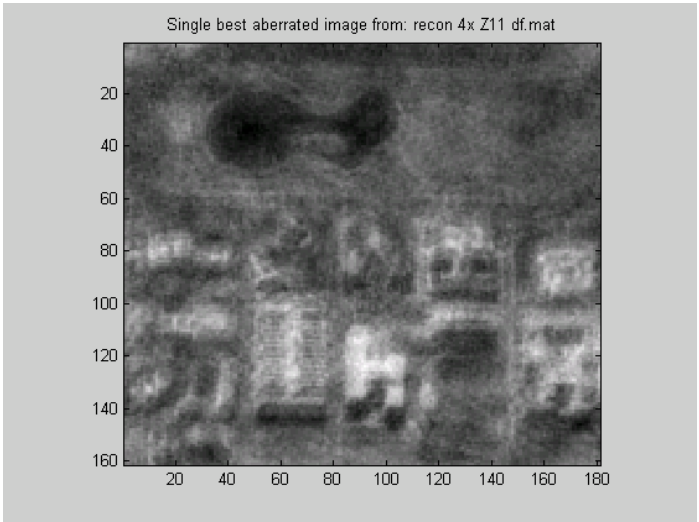

Figure 8. Simulated Image of the Single Best Focus Setting for 4/14 Waves of Zernike Aberration 11 (Spherical).

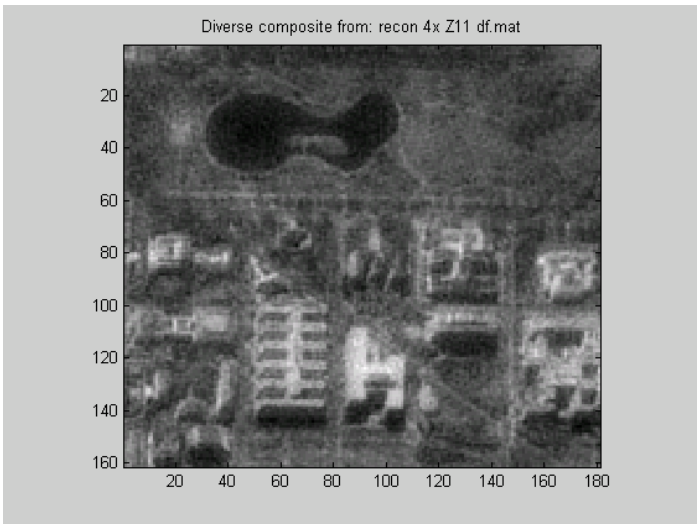

Figure 9. Simulated Image of Defocus Phase Diversity for 4/14 Waves of Zernike Aberration 11 (Spherical).

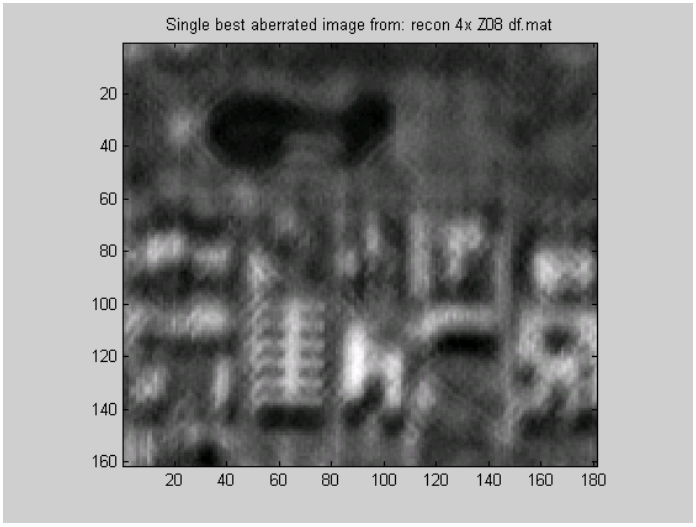

Figure 10. Simulated Image for the Single Best Focus Setting for 4/14 Waves of Zernike Aberration 8 (Coma).

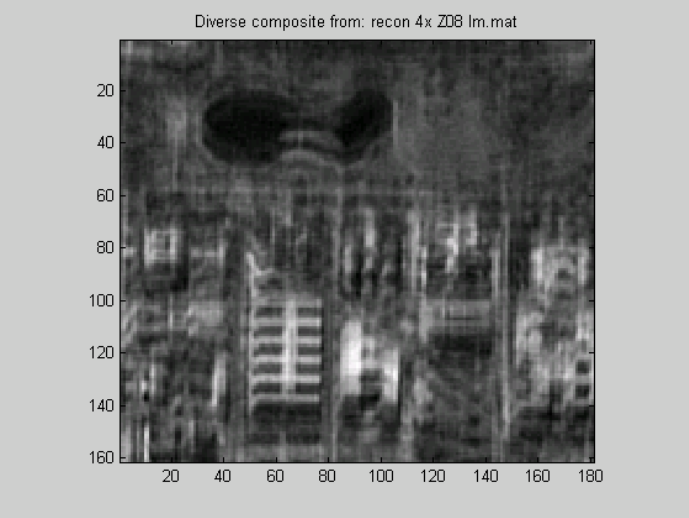

Figure 11. Simulated Image for Low Mode Set of Phase Diversity for 4/14 Waves of Zernike Aberration 8 (Coma).

Figure 8 shows the scene as it would appear with 4/14 waves of Zernike aberration 11 (spherical aberration) after reconstruction at the single best focus setting. Figure 9 shows the scene with spherical aberration reconstructed using defocus diversity. According to Figure 5, defocus phase diversity will produce essentially the same result as will the low-mode set of generalized phase diversity for spherical aberration. Figure 9 (defocus diversity) shows somewhat greater definition and detail than Figure 8 (best focus). This is especially noticeable with the ribs on the building in the lower left corner of the image, with the features of other buildings, and for the island and border of the lake at the top of the scene.

Figure 10 shows the scene as it would appear with 4/14 waves of Zernike aberration 8 (coma) after reconstruction at the single best focus setting. According to Figure 5, defocus phase diversity will produce essentially the same result as the single best focus for Zernike aberration mode 8. Figure 11 shows the scene reconstructed using the low mode set of generalized phase diversity. Again, the diverse composite image (Figure 11) shows noticeably greater definition and detail than the image acquired at single best focus (Figure 10). The ribs of the building at lower left, details of other buildings, the island and lake, and the triangle of major streets are all more distinct in the diverse composite. However, there does appear to be some ringing in the phase diverse reconstruction. This is especially noticeable for the island, and in general for many of the sharply defined horizontal lines.

4. Design of the Bench Top Optics System

4.1 Overview

A sketch of the basic layout of the optics for the bench top optical system is shown below as Figure 12. The purpose of this optical system was not to demonstrate a scaled down or simplified version of a proposed operational system. Rather this system had the following two main purposes. 1) Produce quantitative image data to validate computer simulations of the diversity imaging concept. 2) Produce images that demonstrate the utility of the diversity imaging scheme. The basic function of the optics is to form an image on a CCD detector of a test pattern and to allow the controlled introduction of both optical aberrations and phase diversity.

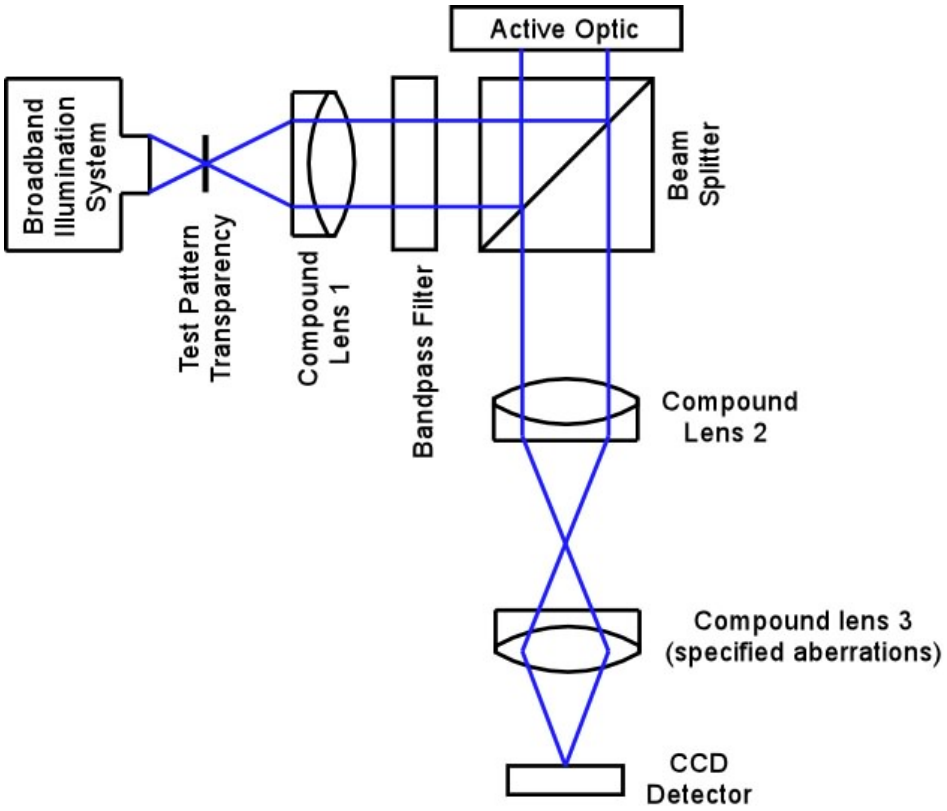

Figure 12. Sketch of the Basic Layout of the Bench Top Optical System.

The system can be broken down into three main functional blocks. The first functional block creates a test pattern that serves as the input object. The second functional block introduces phase diversity using an active optic and re-images the test pattern. This block also includes a band pass filter to restrict the spectral range of the system. The third functional block produces a final image of the test pattern on the CCD array detector and permits the controlled introduction of aberrations. Each of these functional blocks is described in more detail below.

4.2 Block 1

The first functional block is a broadband illumination system plus test pattern transparency, which together produce the input object to the imaging system. The broad band illumination

source is a quartz-tungsten-halogen lamp plus a condenser lens. A sinusoidal target was used to make direct measurements of the system's modulation transfer function (MTF). The sinusoidal target was item A55-641 from Edmund Industrial Optics, which is a 1-inch x 3-inch slide with sinusoidal patterns ranging from 2 to 256 line pairs per mm (lp/mm). The USAF 1951 test pattern was used to demonstrate the quality of the images formed by the system. The USAF target was item A38-256 from Edmund, which is a 2-inch x 2-inch slide that contains groups down to 228 lp/mm.

4.3 Block 2

The second functional block includes the following elements: compound lens 1, band pass filter, beam splitter cube, active optic, and compound lens 2. Compound lens 1 produces a collimated version of the test pattern and compound lens 2 reforms the image at 1:1 magnification. The active optic is a membrane deformable mirror (MDM), which introduces the phase diversity. The beam splitter provides a convenient way to route light to and from the active optic. The beam splitter is a cube to avoid the introduction of unwanted aberrations. Compound lens 2 is a reversed version of compound lens 1. The band pass filter limits the spectral band pass of the system, in order to preserve diffraction effects in the final image. The baseline band pass is 608-658 nm, which is centered on the helium neon (HeNe) laser line at 632.8 nm. (Although the system was normally illuminated with broad band light, it was convenient to work with a HeNe laser for certain test purposes). The aperture stop for the system will be set as near to the active optic as possible. All elements in this functional block are arranged symmetrically around the aperture stop, to permit easy aberration correction from lenses 1 and 2.

4.4 Block 3

The third functional block includes lens 3 and the CCD detector. Lens 3 forms the final image of the test pattern on the CCD detector. :ens 3 is a triplet that produces close to diffraction-limited imagery. This serves as a direct standard of comparison for the performance of the diversity imaging technique after aberrations are introduced. Spherical aberration was introduced by adding a zero power doublet lens after lens 3. This doublet was shifted off-axis to produce coma. A weak cylindrical lens introduced astigmatism.

4.5 Sampling and Resolution Parameters

The CCD camera is a 1280 x 1024 array of 6 x 6 μm pixels. The diameter of the Airy disk for the system was set so that pixels on 6 μm centers produce Nyquist sampling at the incoherent cutoff frequency. The incoherent cutoff spatial frequency for a diffraction limited system is[6]

$$\rho = 2\rho_o = d/\lambda z \,, \qquad (\mathbf{8})$$

where

ρ = incoherent cutoff spatial frequency,

ρ_o = coherent cutoff spatial frequency,

d = diameter of exit pupil,

λ = wavelength, and

z = distance from exit pupil to focal plane.

Nyquist sampling requires sampling at twice this cutoff frequency, $2d/\lambda z$, or a sampling interval of $\lambda z/2d$. This is related to the diameter of the Airy disk by[6]

$$\Phi_A = 2.44\lambda z/d \,, \qquad (9)$$

where

Φ_A = diameter of the Airy disk,

and the other quantities are as defined above. Nyquist sampling thus corresponds to 4.88 samples across the diameter of the Airy disk. This means that an Airy disk diameter of 4.88 x 6 μm = 29.3 μm is required for Nyquist sampling at the incoherent cutoff frequency. An optical design program showed an Airy disk diameter of 29.28 μm for the system as designed. The corresponding incoherent cutoff frequency is $2.44/\Phi_A$ = 83.3 mm^{-1} at the focal plane. The paraxial magnification of the system is 2.7, so the cutoff frequency in the object plane is about 226 mm^{-1}. Under diffraction limited conditions it should be possible to observe some modulation of the highest spatial frequency 3-bar object on the test pattern, which has 228 lp/mm, but the object will not appear as a set of sharp edged lines.

4.6 Object and Image Height Parameters

The maximum image height for design purposes was determined by the size of the CCD array. The 1280 x 1024 array of 6 x 6 μm pixels works out to a 7.68 by 6.14 mm active area, or 9.83 mm along the full length of the diagonal. The optics were optimized out to a maximum image height of 4.92 mm. This image height corresponds to the half FOV, and so the full FOV covers the full length of the diagonal on the CCD. Since the system operates at a linear magnification of 1:2.7, a single frame captures an area of 2.84 by 2.27 mm on the object transparency. Since the smallest set of target bars is 228 lp/mm, this captures several complete groups of elements – certainly out to patterns that are very coarse compared to the system resolution.

4.7 General Requirements on the Active Optic

Note: All wave front and mirror deformations listed in this section are peak-to-valley.

The correction range required from the mirror was calculated assuming that small deformations in the mirror introduce corresponding phase changes in the reflected wave front. This assumption was verified using an optical ray trace program. Preliminary studies indicated that the diversity imaging technique is most useful with up to about five waves of aberration and performance is very degraded with more than about ten waves of aberration. For spherical aberration it was found that a total defocus range of one to two times the waves of aberration was useful. This means that the minimum useful adjustment from the active optic is 5 waves, the maximum that might ever be used is 20 waves, and 10 waves is probably a reasonable compromise. For operation centered on 0.6328 μm, 3.2 μm of wave front deformation is the absolute minimum workable value, 12.7 μm is the potential maximum value, and 6.3 μm is a very comfortable value. Since the phase delay is introduced on both the outgoing and return paths, the mechanical deformation that is required for the mirror is half of the wave front deformation. The system was designed around an Intellite membrane deformable mirror (MDM) with a maximum aperture diameter of 25 mm.

This page intentionally left blank

5. Defocus Measurements made with the Bench Top System

Defocus is the most basic aberration that can be applied to a membrane deformable mirror. Because of its apparent simplicity, it has been little studied, despite the fact that it is ubiquitous in adaptive optics applications. Phase diversity wavefront sensing and non-mechanical zoom are two techniques that depend on defocus for their operation. The purpose of this study was to find out the precision with which defocus can be applied to the mirror, the best actuator voltages to achieve defocus, the resulting focus shape, and the range of defocus.

5.1 Methodology

All of the data reported were taken on a single Intellite 25–37 DM. This is a deformable mirror of standard design, with a 25-mm diameter and 37 actuators arranged in a hexagonal array. The spacing between the pad array and membrane is nominally 40 microns for this design, and for this particular mirror it was measured to be 41 μm.

Membrane deflection was measured with a Polytec Laser Doppler Velocimeter (LDV), which can measure velocity with a resolution of 0.05 um/s/root(Hz) and deflection with a resolution of 2 nm. In practice, the measurement resolution is limited by the acoustic vibrations. To minimize vibrations the LDV sensor head and mirror were both mounted on a vibration damped optical table. The LDV sensor head was mounted to the table at the correct height using a Thor Labs dynamically damped 14-inch mounting post. The mirror was mounted to a Sherline milling stage (to provide 2-D positioning), adapted to sit upright and supported by two triangular brackets. This set-up is shown in Figure 13.

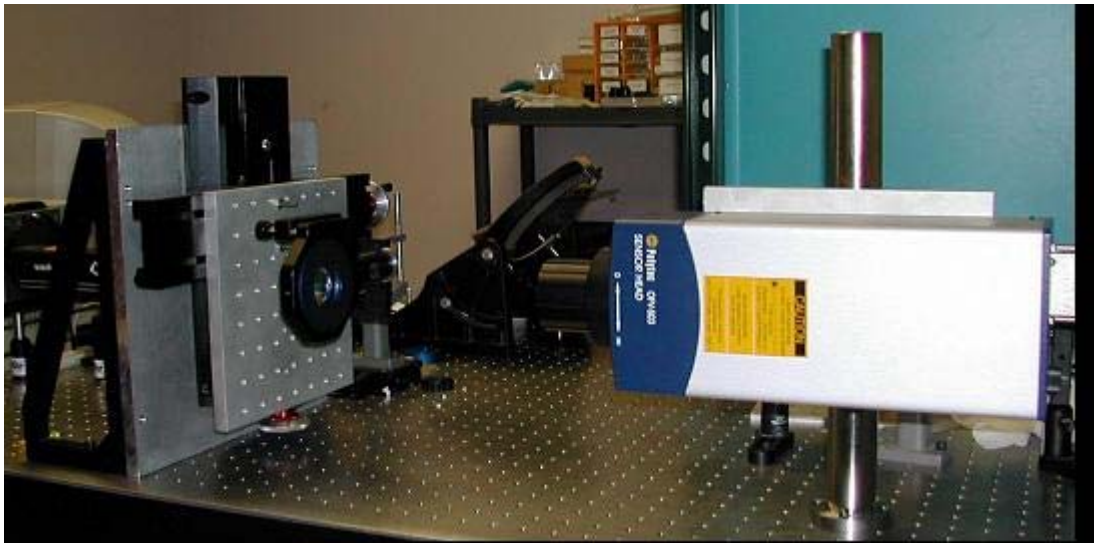

Figure 13. Mounting of the LDV Looking into the Mirror.
The mirror is mounted on a milling stage.

The LDV is equipped with both a velocity and displacement decoder. Both require an AC signal to be applied to the mirror and must be read with an oscilloscope. For this study, the displacement deocoder was used throughout, and set on a scale of 2um/volt. The acoustic vibration noise was limited to 8 mV peak-to-peak at 75 Hz for the displacement decoder on the 2 um/V scale (16 nm). However, the noise was often greater due to low frequency, sporadic events such as footfalls, air-conditioning fans, etc. Hence the noise level varied in time and was hard to quantify.

Another source of uncertainty was variation in the positioning of the milling stage. The position is varied using a hand-wheel (one revolution. /mm) with an estimated uncertainty of about 0.1 mm, but the uncertainty was not measured objectively. An additional source of positioning error in milling stages is backlash, which was minimized by always scanning across the mirror in one-direction.

The mirror was driven by applying voltages to the actuator array. For a singular actuator driven at voltage V, the force F, on the membrane is given by

$$F = \frac{\varepsilon_o V^2 A}{d^2} \ , \qquad (\mathbf{10})$$

where

A = the actuator area, and

d = the spacing between the membrane and the pad array.

The solution for an array of actuators (which may or may not have equal voltages) can be solved using Intellite's DMModel™ software. DMModel also calculates the best actuator array voltages to produce a given aberration. These voltages are the ones that are applied when using the slider bars on the Zernike Window tab of HVDD™, the deformable mirror control software used for these tests. From Eq. 10, one would expect that for a given pattern of actuator voltages, the shape would remain constant if they were scaled (all multiplied by the same factor) with only the amplitude of the aberration changing.

For the first part of this experiment, HVDD was used to drive the mirror with varying amounts of defocus aberration. The voltage patterns used were generated using the Zernike Window tab slider bar. HVDD has a provision to allow cycling between different actuator voltages patterns at a set frequency. The result is a square-wave mirror response that can be read on the oscilloscope. The cycle period used was 500 msec. The LDV displacement decoder has a strong DC drift and, combined with the necessity of DC coupling the oscilloscope for this method, it was not possible to average out any noise. Nevertheless, the bulk of the data was taken this way, because it characterized the defocus obtainable using a standard mirror with our standard method of producing Zernike defocus.

A second way to generate actuator voltages is through a special high band-width amplifier that was built to measure the frequency response of Intellite mirrors. This amplifier uses an arbitrary function generator as an input, and therefore can produce a pure sinusoidal (in time) force on the mirror. The disadvantage is that it can apply only one value of voltage to an entire set of actuators of the users choosing. That Zernike defocus can be accurately produced by applying *the same* voltage to all of the actuators has been speculated about for some time, but never systematically studied. For this experiment, the amplifier was used to apply the same voltage on

all of the actuators and compared the membrane shape to that produced using the HVDD Zernike defocus.

Another advantage of using the amplifier is that the scope can be set to AC coupling and the sine wave input can be split off to be used as a scope trigger to get accurate averaging of the signal. This translates to much less noise in the data.

5.2 Results and Discussion

The deflection of the mirror as a function of position using the HVDD Zernike defocus method is shown in Figures 14a–c. Each graph is for a different focus range for ease of viewing. Data was taken for actuator voltages from 5 to 100 V.

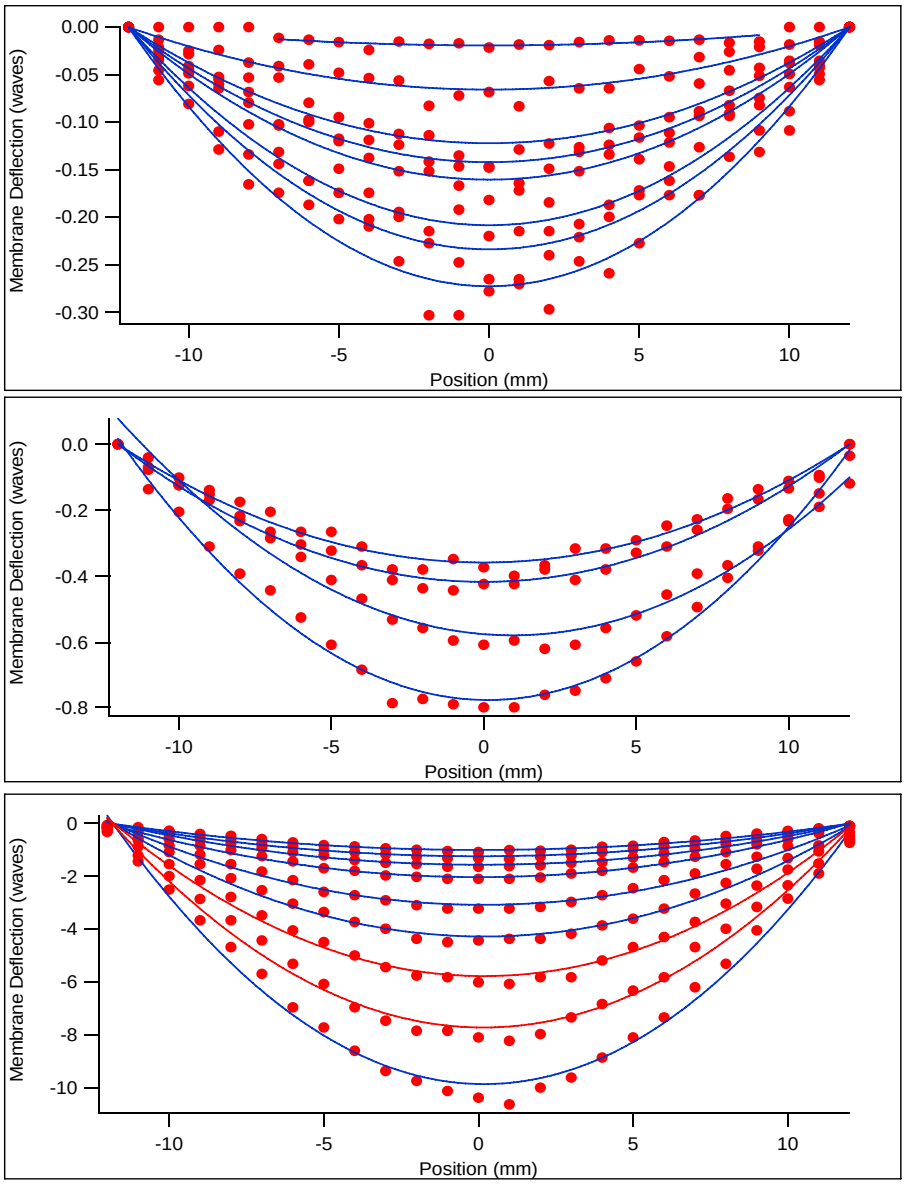

Figure 14 a–c. Membrane Deflection as a Function of Position Across the Mirror.

The blue lines are fits to the function

$$D(x) = A(1 - Bx^2), \tag{11}$$

where

D = the membrane deflection in waves, and

x = the position from left to right across the mirror in millimeters.

B was held fixed in the fit (so that the deflection was always zero at the edge of the mirror) and A recorded as the amplitude of the mirror deflection at the center.

Figure 15 shows A as a function of the maximum actuator voltage (this would be the number that appears in the Zernike Window slider bar). The fit line is to a square law (as in Eq. 10). The error bars are about the size of the data points, so the square law fit is adequate, but not perfect, especially for voltages greater than about 50 V. This plot shows that 9 waves of defocus can be applied to the mirror with a 200-V drive. For voltages less than 100 V, the precision which defocus can be applied is better than /20. Better precision at higher voltages was not demonstrated due to time constraints.

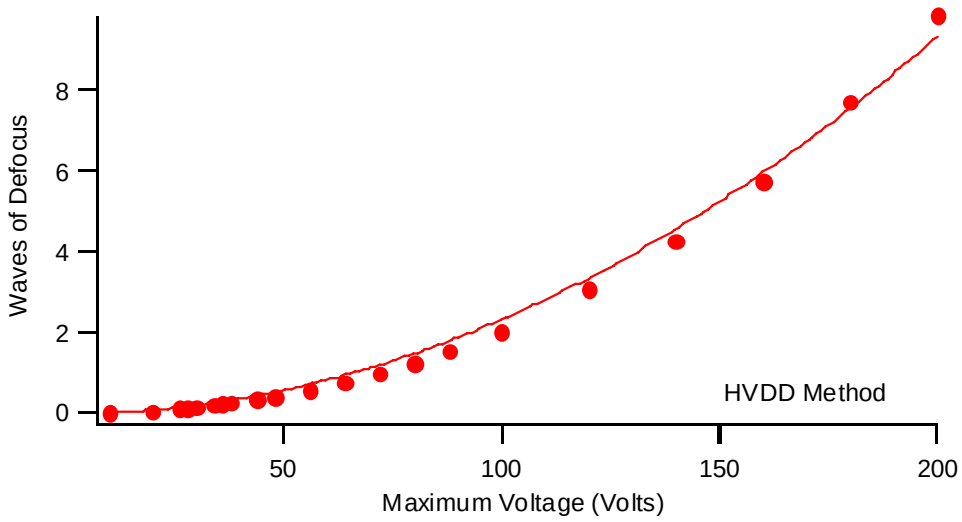

Figure 15. Center Deflection as a Function of Maximum Actuator Voltage.

A typical plot of membrane deflection versus radial position is shown in Figure 16. The fit to defocus (Eq. 11) is, again, adequate.

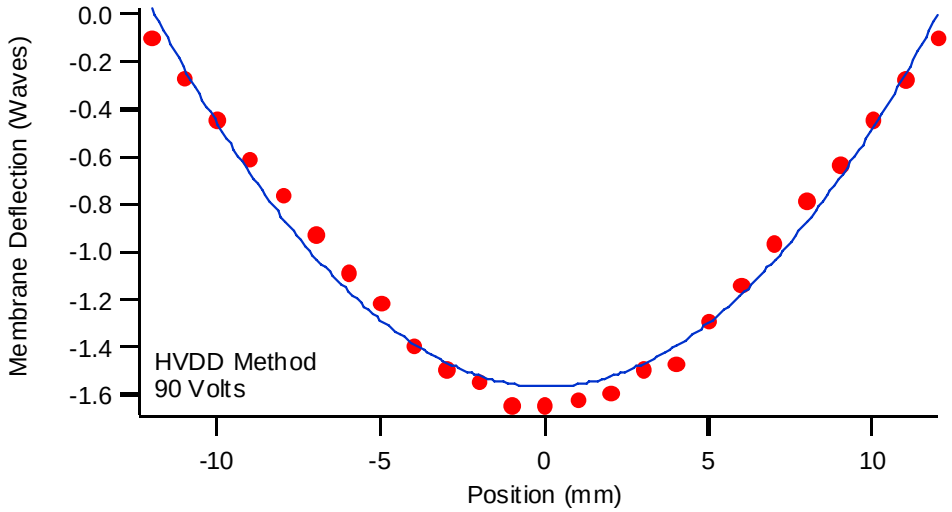

Figure 16. Mirror Deflection versus Position Using the HVDD Method.

Data were then taken using the high bandwidth amplifier, both to get more precise results, and to compare them with the HVDD method. Figure 17 shows mirror deflection versus position using the amplifier. The improvement in signal-to-noise ratio is evident, as well as the quality of the fit to Eq. 11. From this we can conclude that applying the same voltage to all of the actuators is a convenient and accurate way to get defocus. To complete the study, deflection measurements were made at the center of the mirror versus voltage in 2-V increments. The result is shown in Figure 18. The square law fit is beautiful and demonstrates at least /10 precision (/20 in some ranges) for defocus from 0 to 3 waves. Unfortunately, data could not be collected at higher voltages because of amplifier noise.

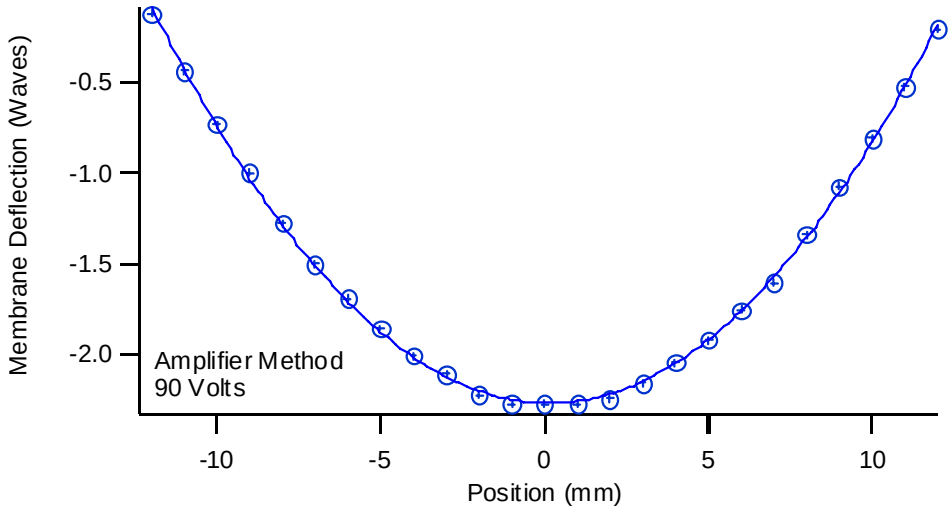

Figure 17. Deflection Versus Position Using the Amplifier, and Applying the Same Voltage to All Actuators.
The defocus fit is near perfect.

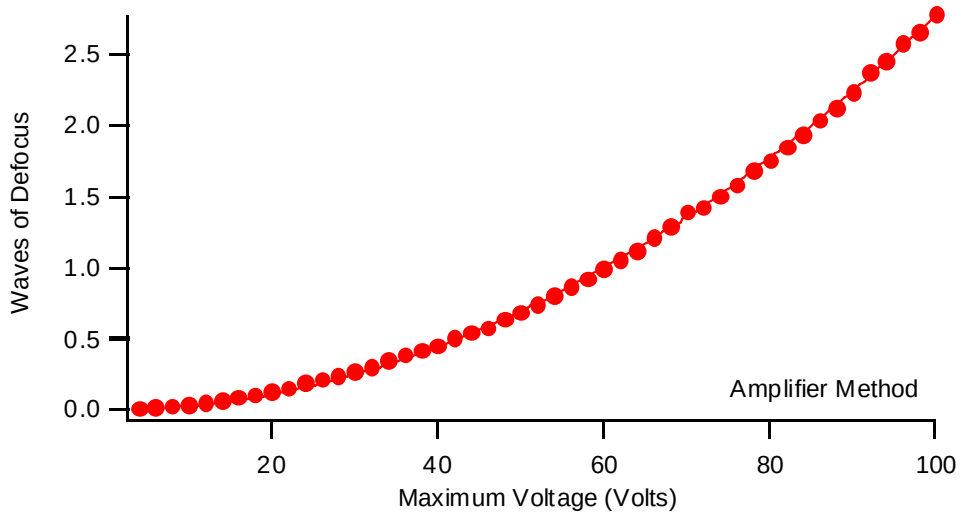

Figure 18. Center Deflection Versus Voltage Using the Amplifier and Applying the Same Voltage to All Actuators.
The fit is to a square law.

5.3 Conclusions Regarding Precision Defocus Measurements

This study of membrane shape and deflection versus applied voltage shows that the dynamic range of the mirror is more than adequate for phase diversity and non-mechanical zoom applications. Moreover, it was shown that Zernike defocus can accurately be obtained by applying equal voltages to all actuators. Data on defocus using DMModel to derive actuator voltages was harder to characterize because of the inability to average the DC-coupled signal. However, adequate S/N was obtained to show that the DMModel voltages produce a less accurate Zernike defocus than applying equal voltages to all actuators, at least over the range of voltages measured for both. It is possible that the DMModel voltages are accurate over a smaller diameter on the mirror, but establishing this was outside the scope of this study.

For further work, it would be interesting to study defocus using the amplifier at higher voltage ranges, as well as to characterize the membrane shapes for both methods more thoroughly. In particular, membrane shapes using the amplifier could be studied over a wider range of voltages. This study could also be extended to other, higher order, aberrations but modifications to the amplifier would be required.

6. Closed-Loop Feedback Control Tests for the Bench Top System

The phase diversity application places severe requirements on the wavefront control of the deformable membrane mirror (DMM). In order to obtain useful information, precise amounts of defocus must be applied without introducing significant amounts of other aberrations. In order to assess commercially available DMMs for this application, we evaluated the wavefront control from both a 37-channel and 59-channel OKO DMM. Our goal was to manually adjust the applied voltage scheme in order to accurately produce a specified amount of defocus while reducing any residual aberrations below the diffraction-limited threshold. However, even with feedback from a Shack-Hartmann wavefront sensor, manually adjusting the mirrors in order to remove residual aberrations and create a simple wavefront with pure focus turned out to be very difficult. We therefore set up a closed-loop compensator, which entailed integrating feedback from an adaptive optics (AO) loop and letting an automated control algorithm converge to a solution.

The optical setup for the closed-loop compensator is shown below in Figure 19. Although there are a number of relay optics in the optical train, the basic arrangement is simply a Michelson interferometer. The system compares the wavefront coming from a DMM to that from a static, diffraction-limited mirror with a known focal length. Wavefronts from each mirror sequentially propagates through a lenslet array, which is located in a pupil plane (the mirror serves as the aperture stop). The lenslet array focuses spots onto a charge coupled device (CCD) camera.

Figure 19. Adaptive Optics Test Bed with the 37-Channel OKO Mirror.

An existing AO feedback control algorithm developed by Narrascape for the NRL was used to generate a solution, Figure 20. With the OKO mirror blocked, a frame grabber takes an image of the spot locations created by the static, diffraction-limited mirror to use as a reference. The static mirror is then blocked and the OKO unblocked, allowing the wavefront from the DMM to propagate through the system. The software then measures the total error between the OKO and reference wavefronts and attempts to correct the OKO based on its knowledge of the influence function of each actuator.

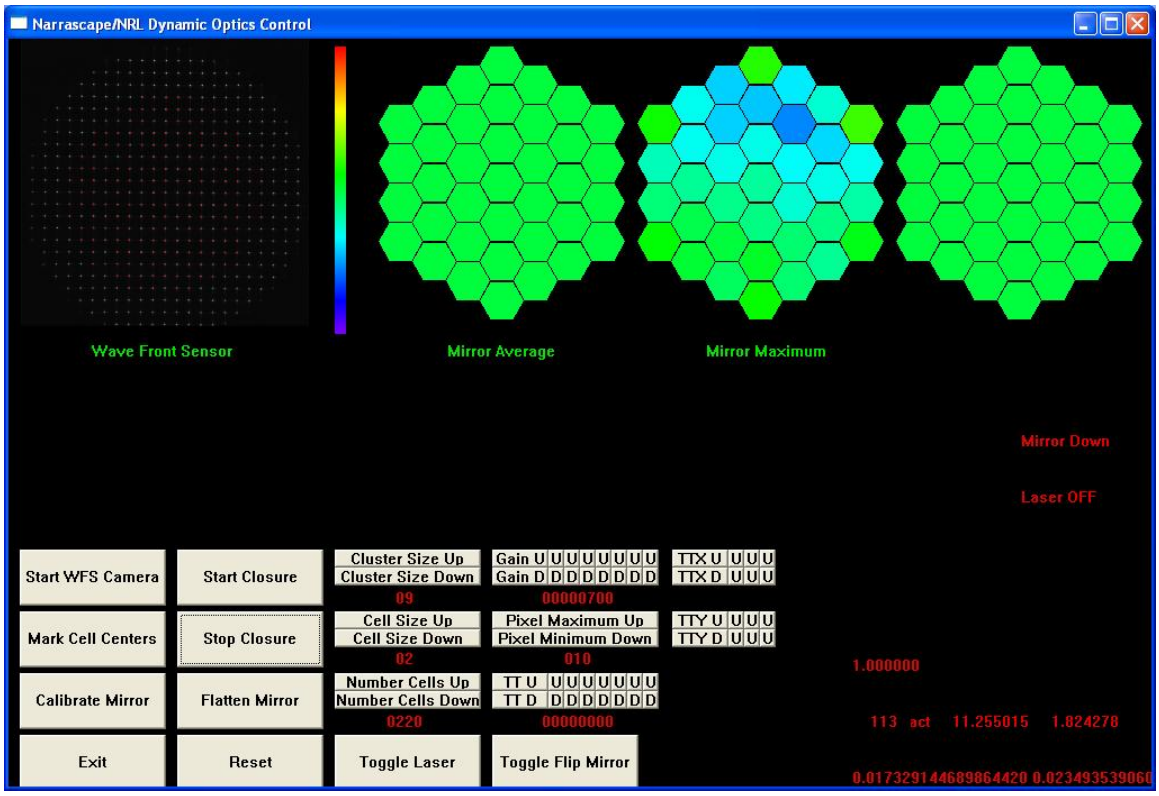

Figure 20. Adaptive Optics Closed-Loop Control Interface for 37-Channel OKO Mirror.

Using a static mirror with a radius of curvature of 5 m (f = 2.5 m) in the reference leg, the control algorithm converged to a stable solution. A color-coded representation of the control voltages that were applied in order to correct the 37-channel OKO are shown as 'Mirror Maximum' in Figure 20 above. When we analyzed this solution, which contained significant amounts of astigmatism, coma, and spherical aberration in addition to defocus, it was easy to understand why it had previously been so difficult to remove aberrations manually.

In order to quantify this solution, we split-off part of the wavefront and relayed it to the commercial Shack-Hartmann wavefront sensor. Again, we used the reference wavefront from the static mirror to verify the overall performance of the optical train. The residual error of the entire system with the reference mirror (f = 2.5 m) had less than 0.25 waves P-V, although there was a significant dynamic contribution due to 1) thermals in the air and 2) vibrations on the table. With the reference mirror blocked and the OKO mirror corrected by the closed-loop compensator, the residual wavefront is also diffraction limited. Notwithstanding the dynamic fluctuations, the residual error nominally had less than 0.25 waves P-V over the central ~80% of

the mirror. Figure 21 below shows the error in the wavefront to be 0.1315 waves. However, the true error is 0.156 waves, as an error was made in entering the reference wavelength.

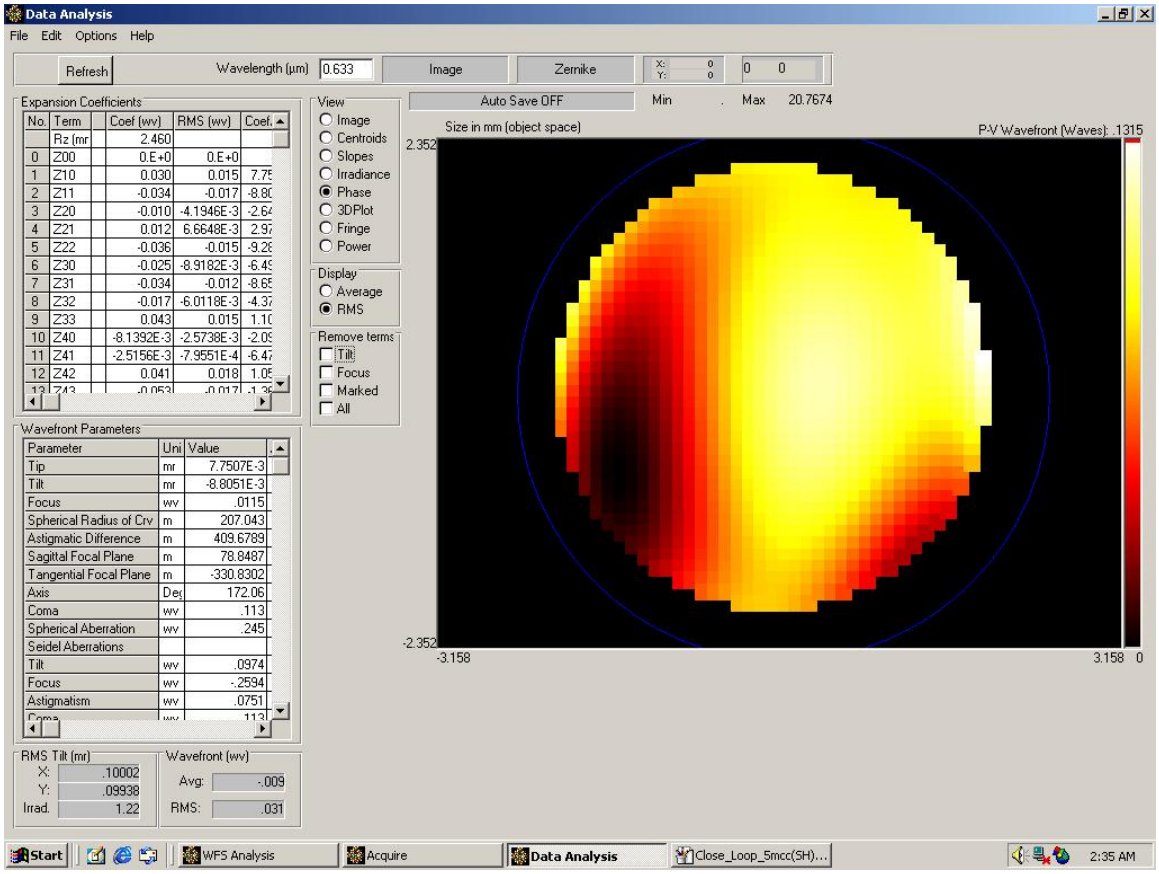

Figure 21. Residual Wavefront Error from the 37-Channel OKO Mirror with f = 2.5 m.

When we let both the reference and OKO wavefronts propagate through the system, we observe interference fringes. An interferogram of the f = 2.5 m reference mirror and the unbiased, "flat" OKO mirror is shown in Figure 22. The bull's-eye pattern shows the defocus that must be applied to the OKO in order to match the curvature of the static mirror. Note that only the 37-channel mirror was able to achieve this amount of defocus. In addition, there is clearly some residual aberration at the edge of these mirrors which will affect imaging capability. In order to reduce this affect, only the central portion of the DMM should be used.

In order to match the mirror figure of the OKO to that of the static mirror, the AO control software starts with a prescribed bias voltage that is applied to every actuator on the mirror. That bias voltage was predetermined through a simple, manual test. Figure 23(a) shows an interferogram when the biased mirror is compared to the static, curved reference mirror. In contrast to Figure 22, we only observe a few waves of residual aberration. As the adaptive optics loop attempts to reach a diffraction limited solution, most of the residual error is eliminated, as seen in 23(b). The wavefront is near diffraction-limited over the central ~80% of the DMM, as shown in Figure 21.

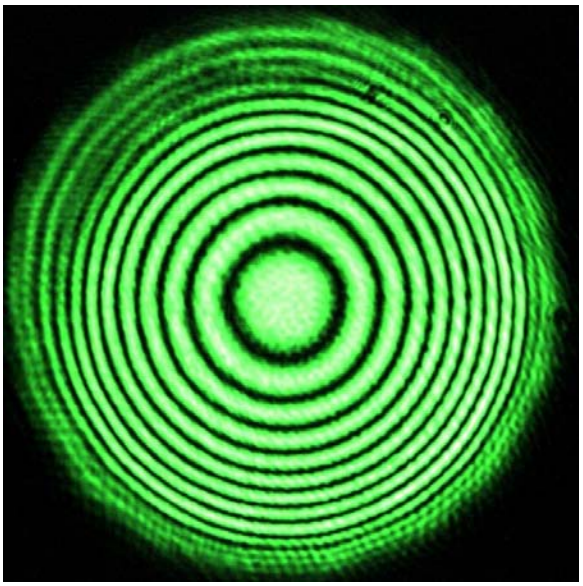

Figure 22. Interferogram from the Unbiased, "Flat" 37-Channel OKO Mirror and a Diffraction-Limited Static Mirror with Focal Length f = 2.5 m in a Michelson Interferometer.

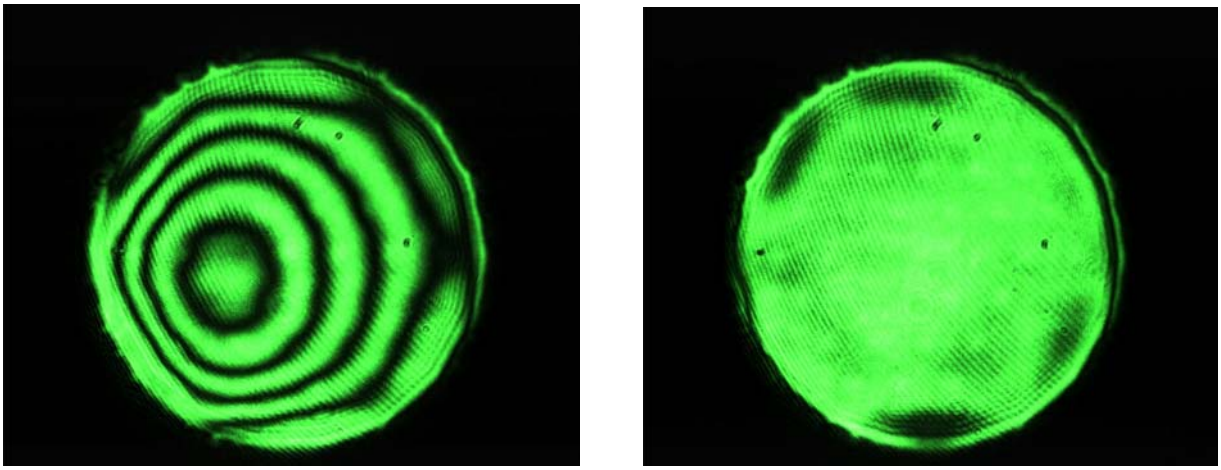

Figure 23. Interferogram from (a) a Biased 37-Channel OKO Mirror and a Static Mirror with Focal Length f = 2.5 m in a Michelson Interferometer.

The bias voltage is determined manually by a first-order, manual estimate. As the closed-loop software approaches a solution in (b), the residual fringes have nearly disappeared.interferometer.

By modifying the control algorithm, we were also able to operate the closed-loop compensator with two 59-channel OKO mirrors. One of the mirrors was capable of matching the curvature of an f = 5 m mirror, but the other was limited to f = 7.5 m. The before and after correction images of the f = 7.5 m mirror are shown below in Figure 24. Again, the central ~70% of the mirror is near diffraction limited after the AO control algorithm reaches a stable solution.

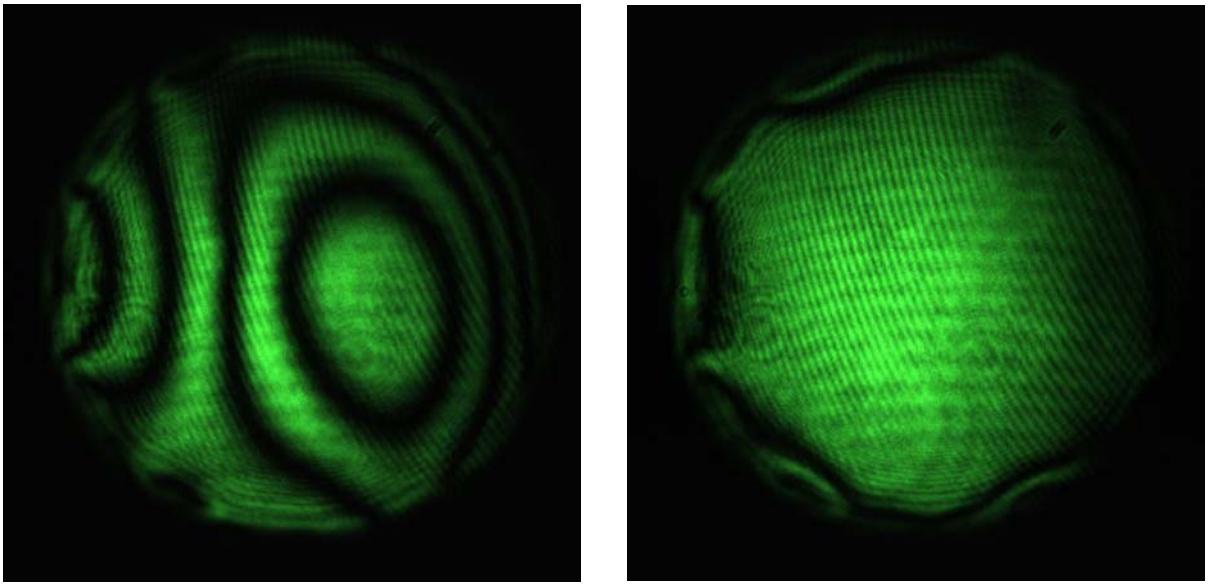

Figure 24. Interferogram from (a) a Biased 59-Channel OKO Mirror and a Static Mirror with Focal Length f = 7.5 m in a Michelson Interferometer.
The bias voltage is determined manually by a first-order, manual estimate. As the closed-loop software approaches a solution in (b), the residual fringes have nearly disappeared.

This page intentionally left blank

7. Summary and Conclusions

This entire study was based on the premise that there can be situations in which residual aberrations remain uncorrected in an adaptive optical system, but that it might still be possible to improve the quality of a reconstructed composite image by applying diverse phase perturbations while multiple images are collected.

The most common implementation of phase diversity is to collect a pair of images, one in focus and one slightly out of focus. It has been shown that the collection of images at multiple settings of defocus can be advantageous when spherical aberration is present.[3] However, the use of defocus fails to improve image quality when coma is present.

It was hypothesized that the use of some type of generalized, non-quadratic phase diversity would be useful when applied to coma and to other aberrations that vary as an odd power of the angular coordinate. A set of low order Zernike polynomials (modes 4, 5, 6, 9, and 10 from Table 1) were identified as a promising set of perturbations to apply for generalized phase diversity. Except for mode 4 (defocus) all of these modes have a zero Laplacian. All of these modes, including defocus, should be relatively easy to implement using a membrane mirror as the active optic.

A merit function based on channel capacity was developed for the purpose of optimizing phase diversity. Optimization was carried out for a variety of specific aberrations. Table 3 summarizes the channel capacity results for Zernike aberrations 8, 11, 12, 14, 16, 18, 20, 22, 24, 26, and 28 for the single best focus, for defocus diversity, and for the low mode set of generalized phase diversity. Various ratios of the results are also shown. All results are for 4/14 waves RMS of the individual aberrations, for a root-squared-sum SNR_{DC} of 100, and for 6 settings when phase diversity is used.

According to Table 3, the biggest improvement from using defocus diversity rather than the single best focus occurs for aberration mode 12. For this case defocus diversity produces a channel capacity that is about 22% larger than the channel capacity at single best focus. The biggest improvement from using the low mode set of generalized diversity rather than the single best focus occurs for aberration mode 24. For this case the generalized diversity increases the channel capacity by about 28%. The biggest improvement from using the low mode set of generalized diversity rather than defocus diversity occurs for mode 8 (coma). For this case the improvement is about 15%. On the other hand for certain aberrations, notably modes 22 and 28, the use of phase diversity produces practically no improvement over the single best focus.

While some of the improvements shown in Table 3 are significant, none are truly outstanding. Furthermore Figure 6 shows that the use of generalized phase diversity rather than the single best focus never fully compensates for the impact of doubling the amount of aberration (except for the one case of 8/14 RMS waves of mode 8, or coma). The general trend of the results of Figure 6 is shown more clearly in Figure 25. Figure 25 uses the same data that is plotted in Figure 6, except that the channel capacity has been averaged over all aberration modes and this average result is plotted as a function of RMS aberration. Figure 25 shows that the low mode set of generalized diversity is on average clearly superior to defocus diversity. However, it also shows a steady degradation of the channel capacity as the amount of aberration is increased, even when generalized phase diversity is used.

Table 3. Channel Capacity (CC) at Single Best Focus (BF), for Defocus Diversity (DD), and for Low Mode (LM) Set of Generalized Phase Diversity for Various Zernike Mode Aberrations.

Each aberration has an amplitude of 4/14 waves. Also shown are ratios of channel capacities for defocus diversity versus single best focus, low mode diversity versus single best focus, and low mode diversity versus defocus diversity.

ABBR. MODE ⇓	CC: BF	CC: DD	CC: LM	DD/BF	LM/BF	LM/DD
8	0.641	0.641	0.735	100%	115%	115%
11	0.538	0.584	0.586	109%	109%	100%
12	0.438	0.537	0.540	122%	123%	101%
14	0.519	0.542	0.579	104%	111%	107%
16	0.543	0.554	0.584	102%	108%	105%
18	0.548	0.549	0.605	100%	110%	110%
20	0.575	0.578	0.646	101%	112%	112%
22	0.622	0.626	0.626	101%	101%	100%
24	0.375	0.438	0.480	117%	128%	110%
26	0.394	0.437	0.444	111%	113%	102%
28	0.556	0.558	0.569	100%	102%	102%
Average	0.523	0.549	0.581	106%	112%	106%
Minimum	0.375	0.437	0.444	100%	101%	100%
Maximum	0.641	0.641	0.735	122%	128%	115%

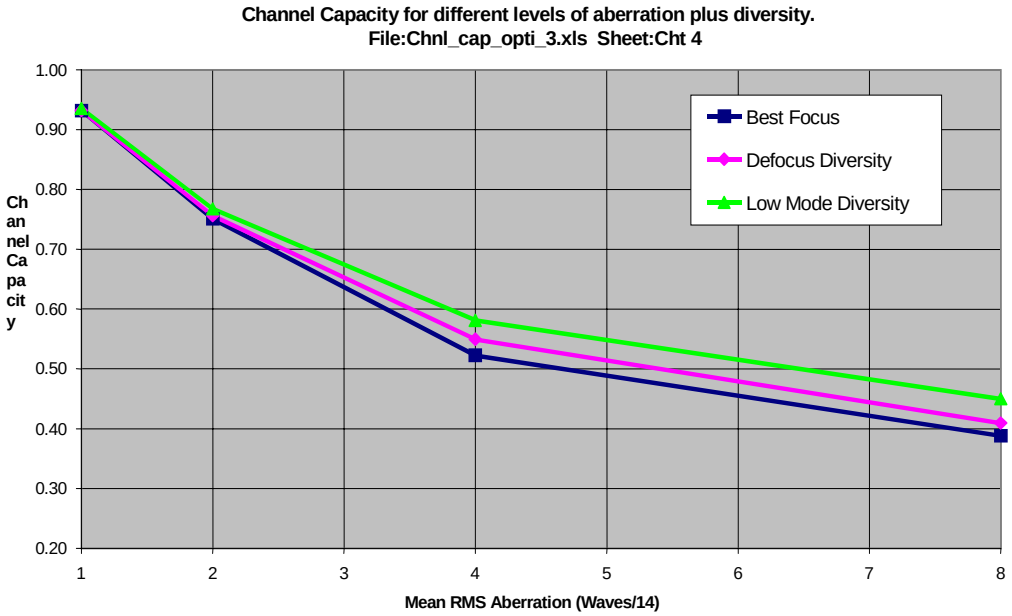

Figure 25. Channel Capacity versus Mean RMS Aberration.

The simulated image reconstructions of section 3.3 included the case of 4/14 waves of Zernike mode 8 (coma), which presents one of the strongest cases for using generalized diversity rather than simple quadratic (defocus) diversity. The image reconstruction results do show an improvement when generalized, non-quadratic phase diversity is applied to coma. However, according to Table 2 the entire improvement is due to a single setting of the phase perturbation, and not to multiple, complementary settings. This suggests that the improvement in image quality for this particular case is due to a partial compensation of the coma, rather than to phase diversity per se.

The various aberrations were studied individually, rather than as compound mixtures. Mixed aberrations are the rule for real optical systems. However, it seems doubtful that applying generalized phase diversity to mixed modes of aberration will produce results that are vastly superior to those derived for individual aberrations.

Overall the results suggest that while phase diversity does have some utility when it is used to enhance the MTF of an aberrated optical system, there is probably more to gain by using active optics to compensate directly for aberrations. As Figure 25 shows, cutting the amount of aberration in half produces a bigger increase in channel capacity than is produced by collecting phase diverse images, even when generalized phase diversity is used rather than simple defocus diversity.

This page intentionally left blank

References

1. R. A. Gonsalves, “Phase Retrieval and Diversity in Adaptive Optics,” *Opt. Eng.* **21**, pp. 829–832 (1982).
2. S. M. Jefferies, M. Loyd-Hart, E. K. Hege, and J. Georges, “Sensing Wave-front Amplitude and Phase with Phase Diversity,” *Appl. Opt.* **41**, pp. 2095–2102 (2002).
3. M. W. Smith, “Simulated Performance of an Optical System That Uses Deconvolution of Multiple, Phase Diverse, Aberrated Images,” *Proc. SPIE* **5174**, pp. 60–68 (2003).
4. M. W. Smith, “Use of Adaptive Optics to Implement Non-quadratic Phase Diversity Imaging,” *Proc. SPIE* **5524**, pp. 66-77 (2004).
5. M. W. Smith and D. V. Wick, “Comparison of Different Modes of Phase Diversity Imaging with Adaptive Optics,” *Proc. AMOS conference* **Vol. TBD**, pp. TBD (2004).
6. J. W. Goodman, *Introduction to Fourier Optics*, Classic Textbook Reissue, pp. 57–62, 65, and 120, McGraw-Hill, New York, New York (1988).
7. F. T. S. Yu, *Entropy and Information Optics*, pp. 22–30, Marcel Dekker, Inc., New York, New York (2000).
8. M. Born and E. Wolf, *Principles of Optics, 7th Edition*, pp. 527–528, Cambridge University Press, Cambridge, United Kingdom (1999).
9. W. C. Elmore and M. A. Heald, *Physics of Waves*, pp. 50–65, Dover Publications, Inc., New York, New York (1985).
10. L. P. Yaroslavsky and H. J. Caulfield, “Deconvolution of Multiple Images of the Same Object,” *Appl. Opt.* **33**, pp. 2157–2162 (1994).

Distribution

1	MS0570	Mark W. Smith
1	0972	C. Andy Boye
1	1188	David V. Wick
1	9018	Central Technical Files, 8945-1
2	0899	Technical Library, 9616